Surface-Specific Deposition of Catalytic Metal Nanocrystals on Hollow Carbon Nanospheres *via* Galvanic Replacement Reactions of Carbon-Encapsulated MnO Nanoparticles

Dong-Gyu Lee,[†,§] Soo Min Kim,[†,§] Hwakyeung Jeong,[‡] Jongwon Kim,[‡,*] and In Su Lee[†,*]

[†]Department of Chemistry, Pohang University of Science and Technology (POSTECH), Gyeogbuk 790-784, Korea and [‡]Department of Chemistry, Chungbuk National University, Chungbuk 361-763, Korea. [§]D.-G.L. and S.M.K. contributed equally to this work.

ABSTRACT This paper reports the findings of our efforts toward gaining a more complete understanding and utilization of galvanic replacement reactions involving manganese oxide with noble metals. It was revealed that the site of metal deposition is significantly affected by the variable oxidation state of manganese oxide. The use of carbon-encapsulated MnO nanoparticles as a reaction template led to metal growth specifically on the outermost surfaces of the carbon shells rather than on the MnO cores, which allowed for the selective decoration of the external surfaces of hollow carbon nanospheres with catalytic nanocrystals of various noble metals, including Pt, Pd, Rh, and Ir. By rearranging the sequence between carbon-shell coating and galvanic replacement processes, the deposited metal nanocrystals could be placed on the interior surfaces of hollow carbon nanospheres and, moreover, separately on the internal and the external surfaces, which may enable the respective control of the catalytic functionalities of each specific surface.

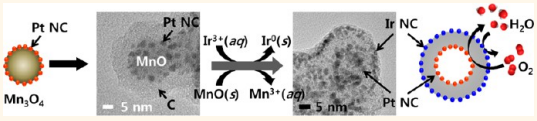

KEYWORDS: hollow nanostructure · metal nanocrystal · catalyst deposition · galvanic replacement · carbon

Hollow carbon nanospheres (HCNSs) are receiving increasing attention as catalyst supports because they integrate the useful properties of carbon,[1−3] including high electrical conductivity and chemical inertness and the distinct characteristics that accompany the hollow morphology, including large surface area and interior void space;[4−6] these properties endow supported metal catalysts with enhanced mass activity and substrate selectivity.[7−10] While many efforts have thus far been devoted to immobilizing catalytic metal nanocrystals on HCNSs, most are restricted to either the interior or the exterior surface; thus, methods for controlling the location of deposition of the nanocrystals remain rare.[11−15] This paper presents an approach for separately decorating the outer and internal surfaces of HCNSs with catalytic nanocrystals; it exploits the effect of the variable oxidation state of manganese oxide on reaction behavior during galvanic replacement with noble metal ions.

We previously reported a method that used electroless metal deposition to immobilize high densities of noble metal nanocrystals on Mn_3O_4 nanoparticles[16,17] *via* a galvanic replacement reaction with metal ions.[18,19] Since the MnO phase of MnO@Mn_3O_4 nanoparticles immediately dissolves during the reaction due to the acidic conditions (*i.e.*, pH 4.0), it was determined that the acid-resistant Mn_3O_4 phase was responsible for the metal deposition process. In our attempt to further expand the utility of this deposition process, we discovered that carbon nanoshells rendered the encapsulated MnO phase sufficiently acid-resistant to participate in the galvanic replacement reaction even in acidic metal precursor solutions. Furthermore, in contrast with what was observed for Mn_3O_4 nanoparticles, the

* Address correspondence to jongwonkim@chungbuk.ac.kr, insulee97@postech.ac.kr.

Received for review December 26, 2013 and accepted April 22, 2014.

Published online April 22, 2014
10.1021/nn5020598

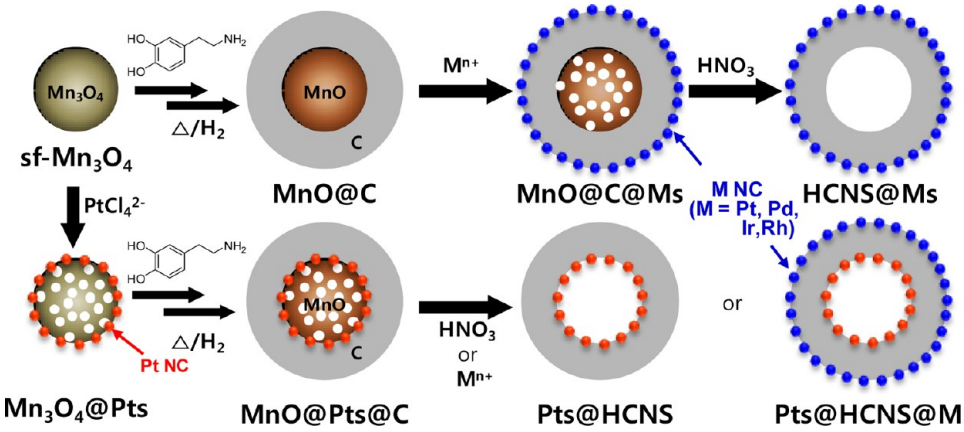

Scheme 1. Protocol of differentially decorating the surfaces of a hollow carbon nanosphere with catalytic metal nanocrystals.

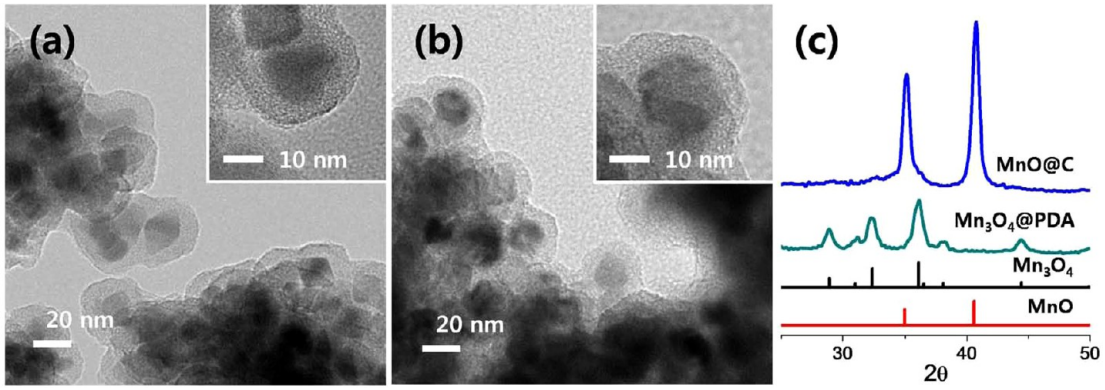

Figure 1. TEM and HRTEM (inset) images of (a) Mn_3O_4@PDA and (b) MnO@C and (c) their XRD patterns. The lines below show the position of the reflections corresponding to tetragonal Mn_3O_4 phase (JCPDS Card No. 80-0382) and cubic MnO phase (JCPDS Card No. 78-0424).

metal growth occurred specifically on the outermost surfaces of the carbon shells rather than on the MnO cores; this allowed selective decoration of the external surface of the HCNSs with catalytic nanocrystals composed of various noble metals, including Pt, Pd, Rh, and Ir. Thus, by rearranging the sequence of the carbon-shell coating and galvanic replacement processes, the metal nanocrystals could be deposited on the interior surfaces of the HCNSs and, moreover, separately on the internal and external surfaces, which may enable specific control of the catalytic functionalities of each surface (Scheme 1). This paper describes the effectiveness of the resulting Pts@HCNS@Irs nanocomposite as a dual-function oxygen electrocatalyst for both oxygen evolution and reduction reactions, with each reaction characterized by the distinct capacities of the Pt and Ir nanocrystals immobilized on the opposite sides of the carbon nanoshells.[20]

RESULTS AND DISCUSSION

Galvanic Replacement Reaction of MnO@C Nanospheres with Metal Ions: Pt Deposition Specifically on the Outer Carbon Surfaces. To prepare the carbon-shell-coated manganese oxide nanoparticles, which were used as the template for the galvanic replacement reaction, surfactant-free Mn_3O_4 nanoparticles were encapsulated with a polydopamine (PDA) film *via* immersion in a Tris buffer solution (pH 8.5) containing dopamine molecules that self-polymerized onto the substrate surfaces at basic pH values.[21,22] A transmission electron microscope (TEM) image of the isolated solids after 24 h of reaction in air revealed Mn_3O_4@PDA nanoparticles with core@shell-type structures and 7.6 (±0.9) nm thick PDA conformal films deposited around the 19 (±3) nm diameter Mn_3O_4 cores (Figure 1a). After annealing the Mn_3O_4@PDA at 500 °C for 5 h under flowing Ar + 4% H_2, the PDA films converted isomorphically into carbon shells (Figure 1b). The analyses of the annealed powder by using X-ray diffraction (XRD), high-resolution TEM (HRTEM), X-ray photoelectron spectroscopy (XPS), Raman spectroscopy, and elementary analysis indicate that the resulting carbon shells were composed mostly of sp^2-bonded amorphous carbon, which incorporated 13% nitrogen atoms (Figure 1c and Supporting Information S1).[23−25] Moreover, the XRD pattern revealed that the carbonization of the PDA shells accompanied a crystalline phase transition of Mn_3O_4 into the more reduced MnO phase, leading to the formation of MnO@C nanoparticles consisting of 19 (±3) nm MnO cores and 7.9 (±0.7) nm thick

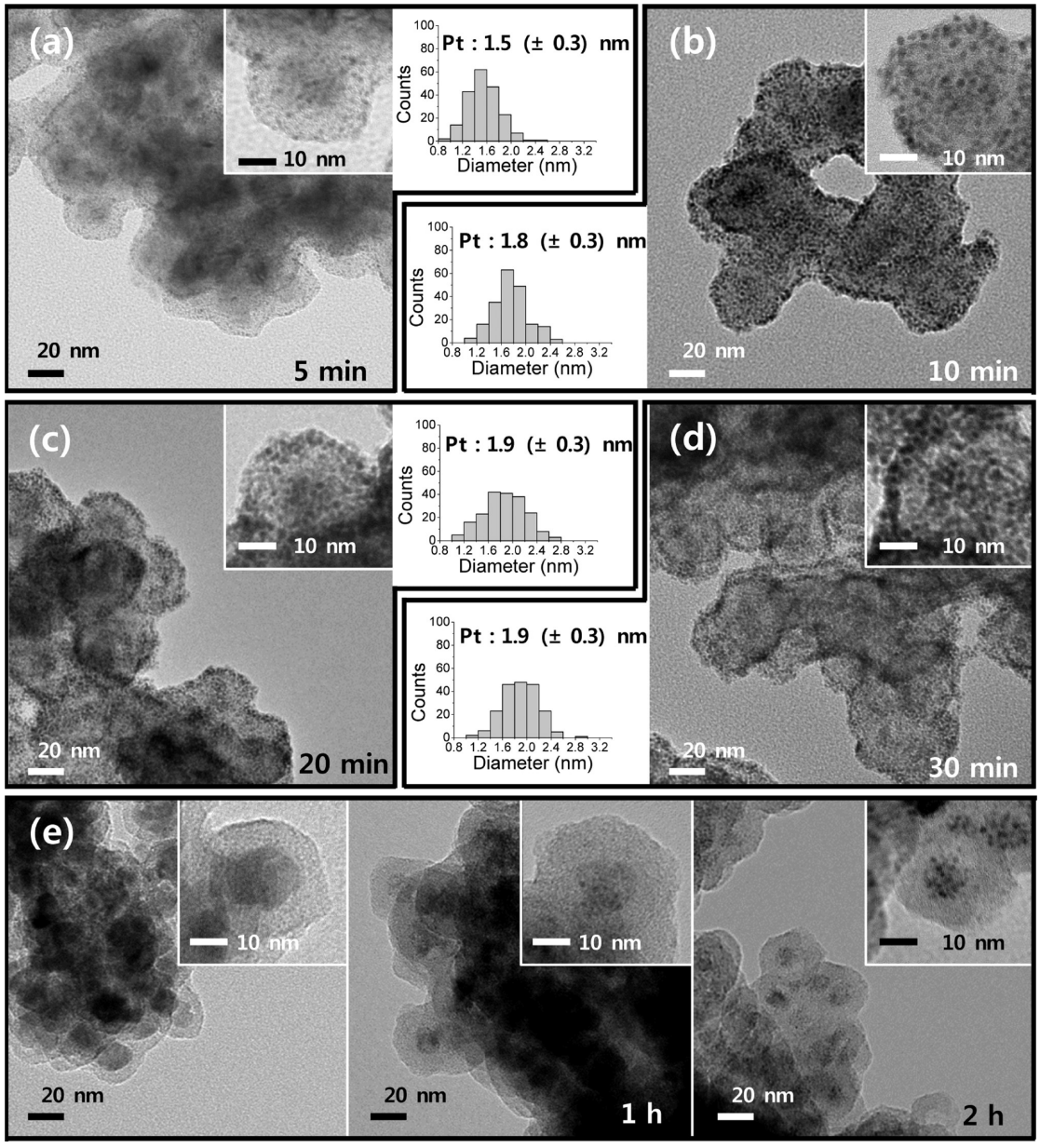

Figure 2. TEM and HRTEM (inset) images of samples obtained by treating the MnO@C in a Na_2PtCl_4 solution for (a) 5 min, (b) 10 min, (c) 20 min, and (d) 30 min at 100 °C. Histograms are showing the size distribution of the deposited Pt nanocrystals. (e) TEM and HRTEM (inset) images of Mn_3O_4@C before (left) and after treating in a Na_2PtCl_4 solution for 1 h (middle) and 2 h (right) at 70 °C.

carbon shells. The observed phase transition of the bulk Mn_3O_4 phase from Mn_3O_4 into MnO, which was not expected at the high reduction temperature of >1300 °C, can be understood in terms of carbothermic reduction reactions between the Mn_3O_4 cores and the PDA-derived carbon shells.[10,26,27]

To investigate the possibility of a galvanic replacement reaction, MnO@C nanoparticles (1.0 mg/mL) were immersed in a Na_2PtCl_4 solution (5.0 mg/mL, pH 3.2) with constant stirring at 100 °C. TEM images of samples obtained from the reaction suspension at different times showed that Pt nucleation and growth on the external carbon surfaces began very early in the reaction, that is, after *ca.* 5 min (Figure 2a). As the reaction proceeded, increasing numbers of Pt nanocrystals were generated exclusively on the outermost surfaces of the MnO@C nanoparticles with a slight increase in their sizes from 1.5 (±0.3) to 1.9 (±0.3) nm between 5 and 30 min of reaction time (Figure 2a–d). It was also evident from TEM and inductively coupled plasma atomic emission spectroscopy (ICP-AES) analyses that the MnO cores progressively dissolved during the reaction, which implied that the Pt growth proceeded at the expense of MnO (Table 1). A control experiment in a HCl solution (pH 3.2) at 100 °C for 12 h did not result in any dissolution of the MnO@C nanoparticles, which illustrated the greatly enhanced acid resistance of the MnO cores that was most likely due to

the surface coating with carbon shells that contained large numbers of nitrogen atoms.[28,29] The improved acid stability due to carbon encapsulation was also verified by a treatment in a more acidic solution (pH 1.4): The MnO@C nanoparticles retained their initial morphology for over 24 h, whereas the MnO cores of $MnO@Mn_3O_4$ and $MnO@SiO_2$ nanoparticles fully dissolved under the same conditions (Figure S2). Immersion of the hollow carbon nanospheres that were prepared by removing the MnO cores from **MnO@C** with Na_2PtCl_4 in a $MnCl_2$ solution or a supernatant solution obtained after treatment of MnO@C in a HCl solution did not result in the formation of metallic Pt species (Figure S3); this indicated that the MnO cores with enhanced stability due to carbon coatings were responsible for the Pt growth on MnO@C. These observations correlate well with the results of our previous investigation of Pt growth on Mn_3O_4 nanoparticles, which proceeded *via* a galvanic replacement process.[17] Accordingly, the deposition of Pt nanocrystals on the MnO@C surfaces was likely a galvanic replacement reaction involving the concomitant reduction of $PtCl_4^{2-}$(aq) to Pt(s) and oxidation of MnO(s) into soluble Mn^{3+}(aq), which is illustrated by eq 1 below.

$$PtCl_4^{2-} + 2MnO(s) + 4H^+ \rightarrow Pt(s) + 2Mn^{3+} + 4Cl^- + 2H_2O \quad (1)$$

Similar to the previous reaction involving surfactant-free Mn_3O_4 nanoparticles, the experiments at lower temperatures, such as 70 and 50 °C, had lower reaction rates and thus less Pt deposition during a given reaction time period; no Pt growth was detected after the reaction at room temperature (Figure S4).

TABLE 1. Mn and Pt Contents in the Supernatant Solution[a]

	5 min	10 min	20 min	30 min	1 h	4 h
Mn	52 μg	110 μg	187 μg	231 μg	281 μg	370 μg
Pt	1.39 mg	1.27 mg	952 μg	723 μg	464 μg	65 μg

[a] Obtained after removing the solid from the 0.5 mL of the suspension for the Pt growth reaction on the MnO@C at different reaction time periods. All the contents were determined by using ICP-AES.

Consideration of the Effect of the Variable Oxidation State of Manganese Oxide on the Galvanic Replacement Reaction. In contrast, Pt deposition distinctively occurred on MnO@C specifically on the outermost surfaces of the surrounding carbon shells rather than on the MnO cores that dominated the galvanic exchange with $PtCl_4^{2-}$. Analogous to Mn_3O_4@C nanoparticles with oxidized phases at the cores, which were prepared by hydrothermal treatment of MnO@C nanoparticles in air and applied to the galvanic replacement reaction

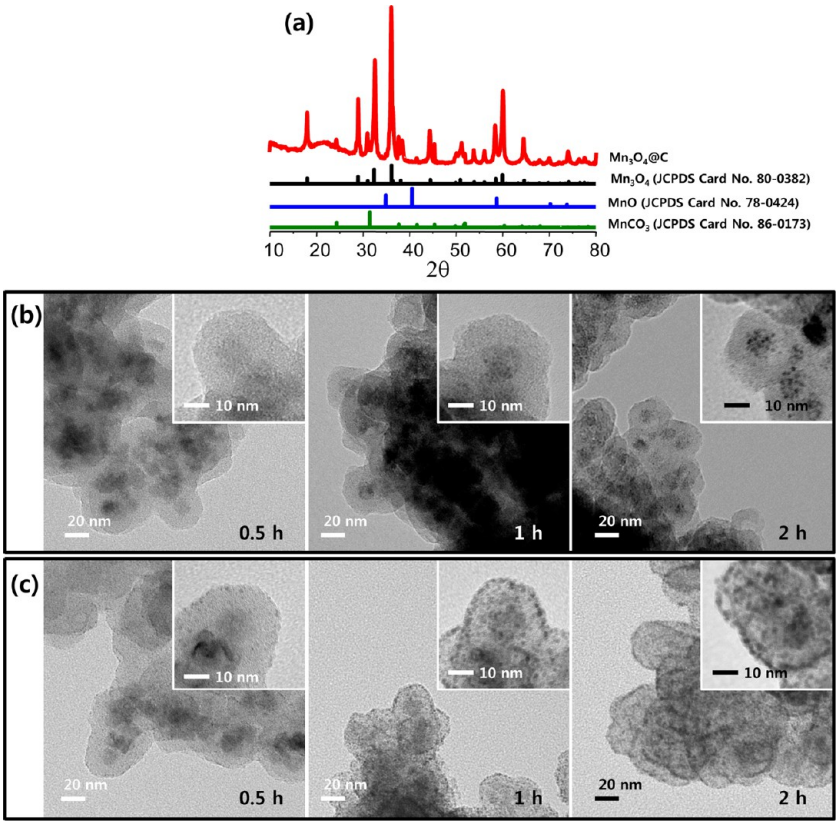

Figure 3. (a) XRD pattern of the Mn_3O_4@C, which was prepared by hydrothermally oxidizing the MnO@C. TEM and HRTEM (inset) images of samples obtained by treating (b) Mn_3O_4@C and (c) MnO@C in a Na_2PtCl_4 solution (1 mg/mL, pH 2.4) at 70 °C for 30 min (left), 1 h (middle), and 2 h (right).

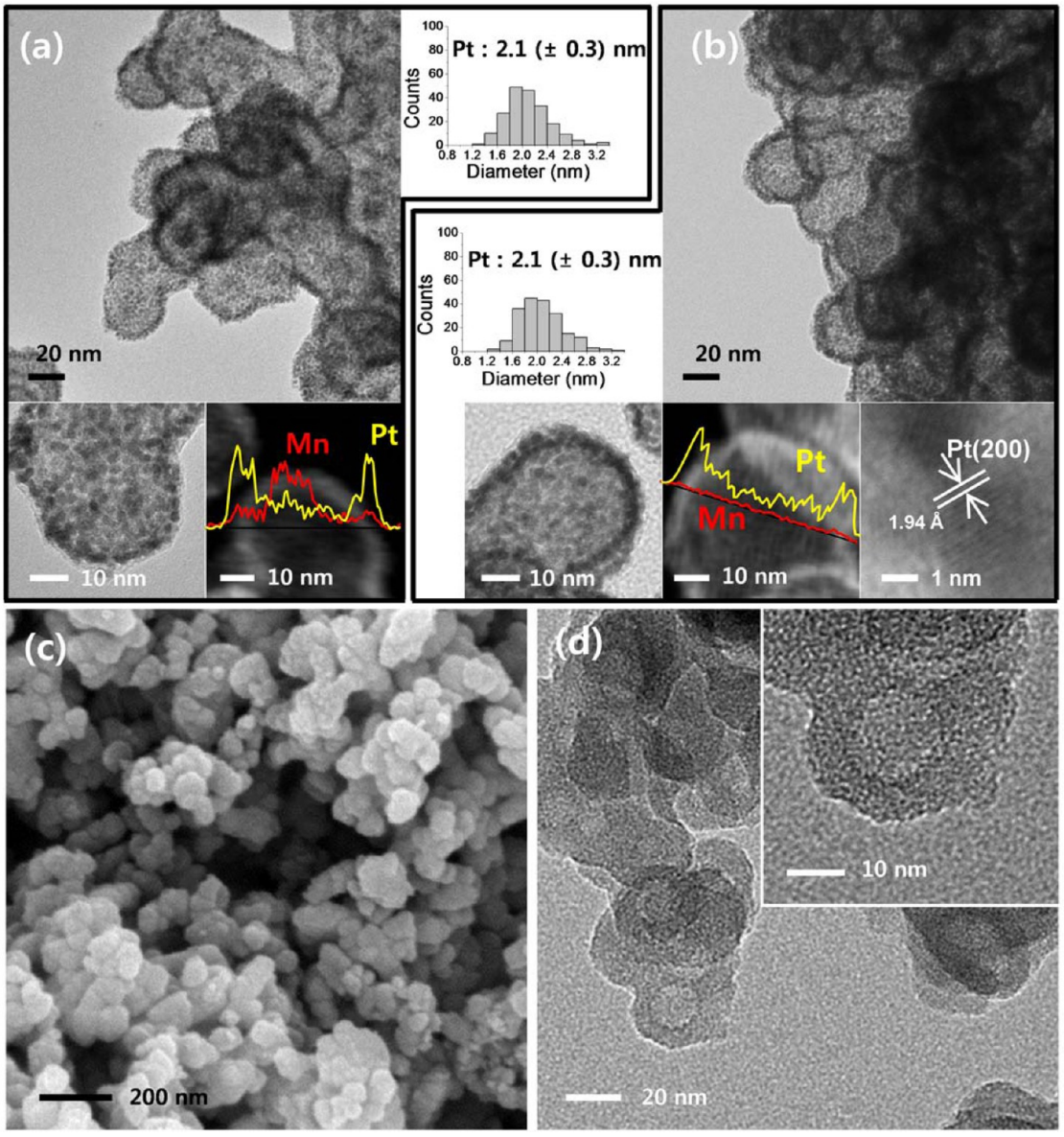

Figure 4. TEM, HRTEM, and STEM-HAADF, which carry the STEM-EDX line profiles for showing the Pt and Mn distribution, images of (a) MnO@C@Pts and (b) HCNS@Pts. Histograms are showing the size distribution of the deposited Pt nanocrystals. (c) SEM images of HCNS@Pts. (d) TEM image of HCNS which was obtained by dissolving the deposited Pt nanocrystals at the surface of HCNS@Pts.

with $PtCl_4^{2-}$, Pt nucleation and growth on these nanoparticles occurred very slowly and only on the Mn_3O_4 cores inside the carbon shells, which is in sharp contrast to the growth observed on the MnO@C nanoparticles (Figures 2 and 3). Although this behavior requires further investigation, such rapid and site-specific Pt deposition on the external carbon surfaces of the MnO@C nanoparticles is best understood based on the much lower standard reduction potential of the MnO(s)/Mn^{3+}(aq) pair rather than that of Mn_3O_4(s)/Mn^{3+}(aq), $\Delta E_{red}^0 = -0.406$ V.[29,30] This difference results in a more positive potential value in conjunction with the reduction of $PtCl_4^{2-}$(aq) during the galvanic replacement reaction with MnO(s) compared to that with Mn_3O_4. This high redox potential enables a galvanic replacement reaction between the redox couples across the carbon nanoshells that involves the reduction of $PtCl_4^{2-}$(aq) to Pt(s) on the outer carbon surfaces *via* the transfer of electrons from the MnO cores through the carbon shells. It was inferred that the carbon shells of the MnO@C nanoparticles, which have high electron conductivity and many defects, played a crucial role in mediating the galvanic reaction by transporting electrons and dissolved Mn^{3+} ions to the surface while retarding the access of $PtCl_4^{2-}$ ions to the MnO core.[31] When a series of MnO@C nanoparticles were prepared with varying carbon-shell thicknesses and then reacted with $PtCl_4^{2-}$ ions under the same conditions, nanoparticles with 4.9 (±0.4) nm and 7.6 (±0.9) nm shell thicknesses both resulted in Pt

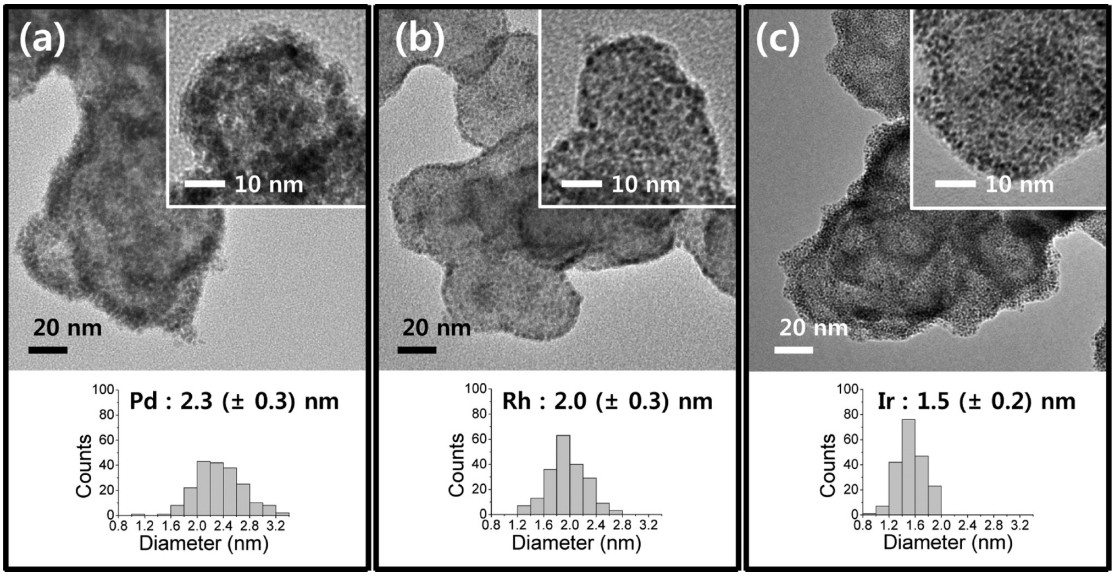

Figure 5. TEM and HRTEM (inset) images of (a) MnO@C@Pds, (b) MnO@C@Rhs, and (c) MnO@C@Irs.

deposition exclusively on the outermost shell surfaces over the whole reaction period. Compared with this, in the case of MnO@C nanoparticles with 3.1 (±0.3) nm thick carbon shells, time course TEM images showed that Pt deposition began to occur on the internal MnO surfaces at 10 min and, as the reaction proceeded, spread over both the carbon shells and the MnO surfaces. These observations suggest that a thickness greater than 3 nm is required to restrict the galvanic replacement reaction to the external surfaces of the carbon shells by hindering the access of the $PtCl_4^{2-}$ ions to the MnO cores (Figure S5). Hence, the reaction of the MnO@C nanoparticles with 7.9 (±0.7) nm thick carbon shells in Na_2PtCl_4 solution for 12 h produced a MnO@C@Pts nanocomposite with a core@shell@satellite superstructure containing tiny Pt nanocrystals of 2.1 (±0.3) nm size densely deposited on the external surfaces of the carbon nanoshells that encapsulated the remaining 4.3% MnO cores (Figure 4a).

Selective Decoration of the External Surfaces of HCNSs with High Densities of Catalytic Nanocrystals. The resulting nanocomposite structure of the MnO@C@Pts nanoparticles led us to examine the possibility of surface-specific immobilization of catalytic nanocrystals on HCNSs. Treatment of the MnO@C@Pts nanoparticles in HNO_3 solution (pH 1.0) resulted in complete removal of the remaining MnO cores without significantly affecting the deposited Pt nanocrystals to generate 17 (±3) nm interior cavities with pristine surfaces inside the carbon nanoshells (Figure 4b–d). Thus, we produced the targeted HCNS@Pts nanoparticles with external surfaces that were selectively functionalized with a high density of ultrafine Pt nanocrystals that have a high potential for electrocatalytic applications.[32–35] The site specificity of Pt deposition on the outermost surfaces was confirmed by TEM, HRTEM, scanning electron microscopy (SEM), and energy-dispersive X-ray (EDX) spectroscopy line profile analyses of the HCNS@Pts nanoparticles. The current procedure was also applicable to immobilization of catalytic species other than Pt; for example, immersion of the MnO@C nanoparticles in Na_2PdCl_4, $RhCl_3$, and $IrCl_3$ solutions led to the deposition of Pd, Rh, and Ir nanocrystals with sizes of 2.2 (±0.4), 2.0 (±0.3), and 1.6 (±0.2) nm, respectively, on the external carbon surfaces through the galvanic replacement process (Figure 5). Subsequent dissolution of the MnO cores from the resultant MnO@C@Ms nanoparticles produced HCNS@Ms (M = Pd, Rh, and Ir) nanocomposites that featured high densities of catalytic nanocrystals of various noble metals immobilized specifically on their outermost surfaces (Figure 6).

Decoration of the Interior and Exterior Surfaces of HCNSs with Either the Same or Different Catalytic Nanocrystals. Following the successful validation of the outer surface-specific immobilization of catalytic nanocrystals, we investigated a method for selectively decorating the interiors of the HCNS surfaces. Accordingly, surfactant-free Mn_3O_4 nanoparticles were first ornamented with 2.0 (±0.3) nm Pt nanocrystals *via* a galvanic replacement reaction and then overlaid with PDA-derived carbon shells using the same carbon-coating procedure applied to the MnO@C nanoparticles (Figure 7a,b). A TEM image of the product, MnO@Pts@C, shows a nanocomposite structure with 2.8 (±0.6) nm Pt nanocrystals, which increased slightly in size during calcination, immobilized at the interfaces between the MnO cores and carbon shells (Figure 7c). Removal of the MnO cores, which had shaped and supported the hollow shells during carbonization, from the MnO@Pts@C nanoparticles with HNO_3 solution resulted in Pt nanocrystals attached to the newly created cavity surfaces of the hollow carbon shells, thereby generating the Pts@HCNS nanoparticles in which only the interior surfaces were inlaid with catalytic Pt nanocrystals (Figure 8a). In addition, this procedure could be further

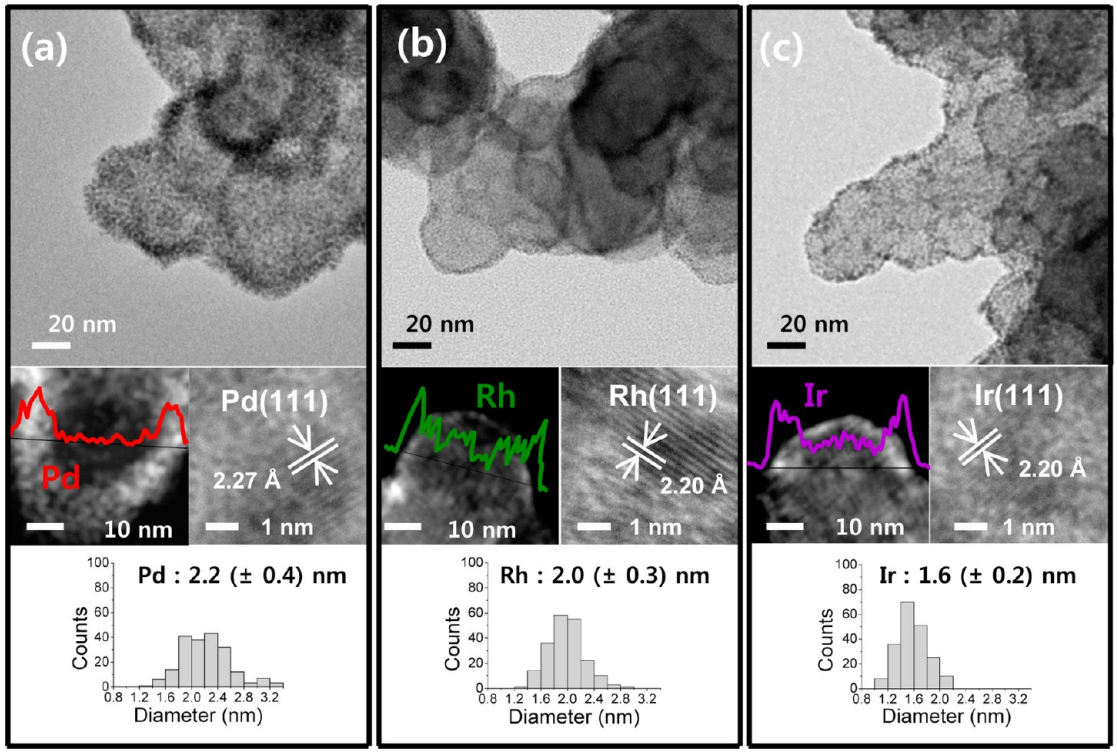

Figure 6. TEM and STEM-HAADF, which carry the STEM-EDX line profiles for showing the distribution of noble metal elements, images of (a) HCNS@Pds, (b) HCNS@Rhs, and (c) HCNS@Irs. Histograms are showing the size distribution of the deposited noble metal nanocrystals.

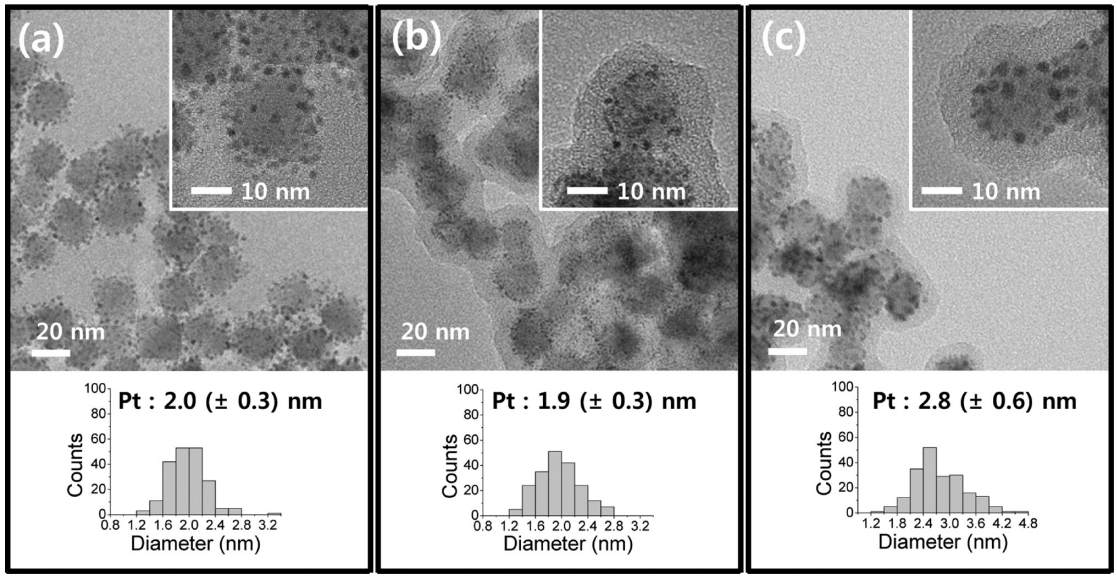

Figure 7. TEM and HRTEM (inset) images of (a) Mn_3O_4@Pts, (b) Mn_3O_4@Pts@PDA, and (c) Mn_3O_4@Pts@C. Histograms are showing the size distribution of the deposited Pt nanocrystals.

expanded as a method for respectively functionalizing the interior and exterior surfaces of HCNSs with either the same or different catalytic nanocrystals. Immersion of the MnO@Pts@C nanoparticles in Na_2PtCl_4 solution resulted in deposition of additional Pt nanocrystals on the outer surfaces, with complete dissolution of the MnO inside the carbon shells. Therefore, the interior and exterior surfaces of the resulting Pts@HCNS@Pts nanoparticles were identically decorated with Pt nanocrystals (Figure 8b). Furthermore, Pts@HCNS@Ms (M = Pd, Rh, and Ir) nanocomposties, whose interior and exterior surfaces were functionalized with Pt and other catalytic metal nanocrystals, were successfully fabricated by reacting MnO@Pts@C nanoparticles with Na_2PdCl_4, $RhCl_3$, and $IrCl_3$ solutions (Figure 8c–e).

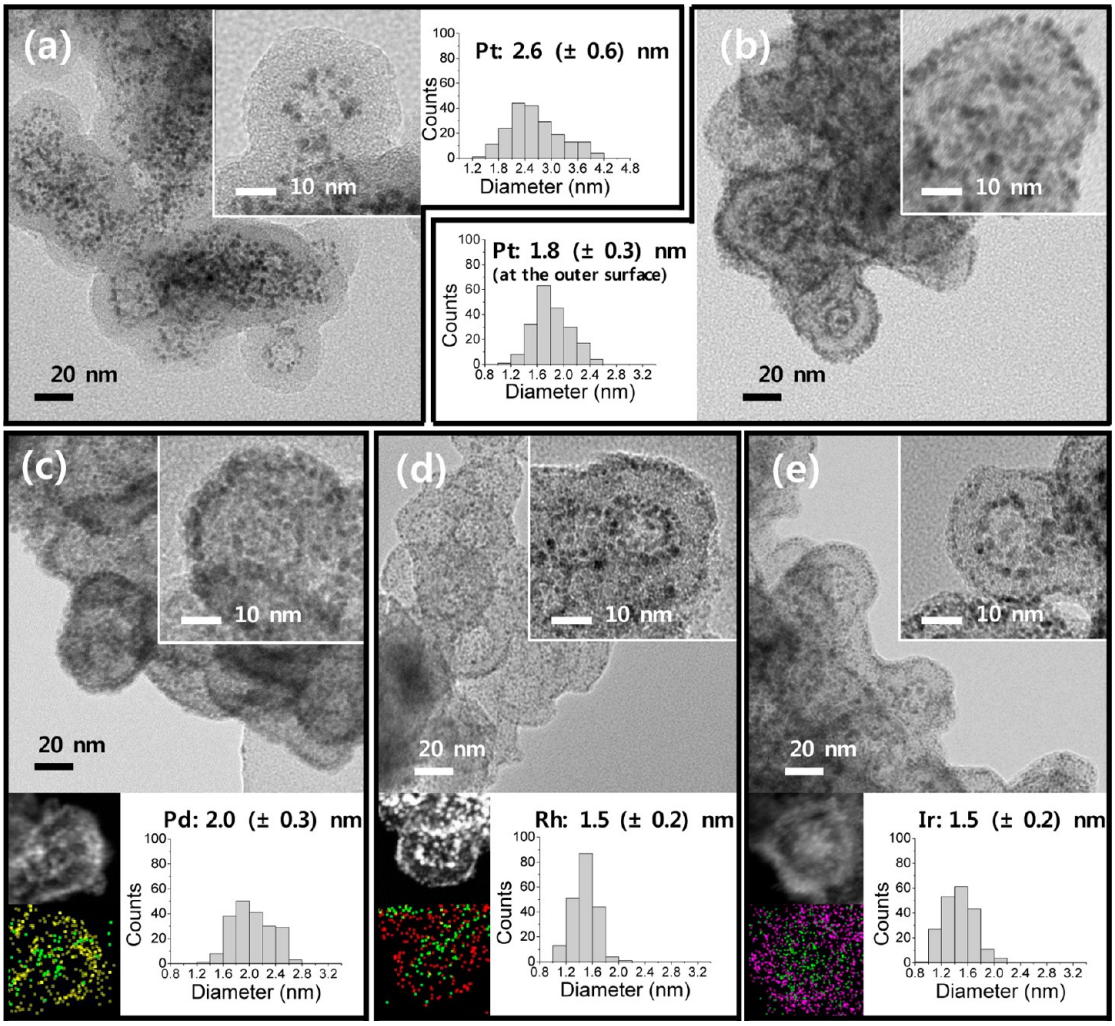

Figure 8. TEM and HRTEM (inset) images of (a) Pts@HCNS, (b) Pts@HCNS@Pts, (c) Pts@HCNS@Pds, (d) Pts@HCNS@Rhs, and (e) Pts@HCNS@Irs. Histograms are showing the size distribution of the deposited metal nanocrystals. Images at the lower left of (c–e) are STEM-HAADF images and elementary maps (Pt, green; Pd, yellow; Rh, red; Ir, magenta) of Pts@HCNS@Pds, Pts@HCNS@Rhs, and Pts@HCNS@Irs, respectively.

Evaluation of Dual Electrocatalytic Performance of Pts@HCNS@Irs. To prove the utility of Pts@HCNS@Ms, retaining different catalytic functionalities at each surface, we examined the electrochemical activities of Pts@HCNS@Irs as bifunctional catalysts for oxygen reduction reaction (ORR) and oxygen evolution reaction (OER). The electrocatalytic activities for these reactions are important for the operation of unitized regenerative fuel cells.[36,37] Figure 9a compares the linear sweep voltammograms of three catalysts for ORR in O_2-staurated 0.1 M $HClO_4$ solutions on a glassy carbon rotating disk electrode (RDE) loaded with each catalyst. The ORR polarization curves indicate that the Pts@HCNS@Irs catalysts exhibit electrocatalytic activity for the ORR that is slightly better than that of the commercialized Pt/C catalysts, which demonstrates that the Pt catalysts deposited in interior surfaces of HCNSs are electrocatalytically active for ORR. The electrochemically active surfaces area (ECSA) estimated from the charge under hydrogen adsorption in cyclic voltammograms (Figure S6) revealed that the ECSA of Pt catalyst at Pts@HCNS@Irs and Pt/C had the same ECSA values. In contrast, the polarization curve of HCNS@(Pt/Ir)s, in which Pt and Ir are co-deposited at the external surfaces of the HCNS, exhibited a negative shift of approximately 70 mV in half-wave potentials compared to the Pts@HCNS@Irs and Pt/C catalysts. This result indicates that the Pt catalysts coexisting with Ir exhibit slower kinetics for ORR. The lower ORR activity on Pt coexisting with Ir at the carbon surface could be attributed to the enhanced adsorption energy of surface oxide at Pt by the interaction between Pt and Ir, which results in the blocking of the active sites for ORR.[38] The stronger adsorption of surface oxides on Pt at HCNS@(Pt/Ir)s could be verified by a positive shift of oxide adsorption–desorption peaks in cyclic voltammogram (Figure S6).[39] Figure 9b shows the linear sweep voltammograms of three catalysts for OER. A significantly higher onset potential was observed at Pt/C compared to those at Ir-containing catalysts,

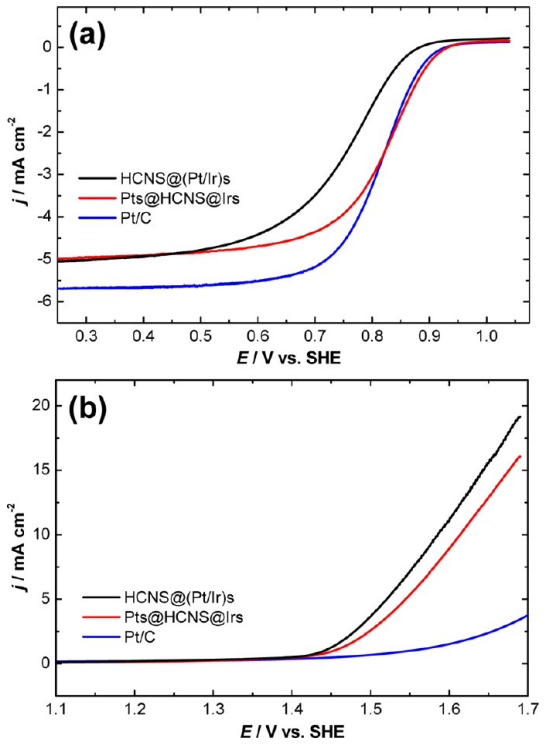

Figure 9. (a) ORR polarization curves of three catalysts obtained in O_2-saturated 0.1 M $HClO_4$ solutions with a scan rate of 10 mV/s and a rotation rate of 1600 rpm. (b) Linear sweep voltammograms for OER obtained in N_2-saturated 0.1 M $HClO_4$ solutions.

indicating lower electrocatalytic activity of Pt for OER. The onset potentials of Pts@HCNS@Irs and HCNS@(Pt/Ir)s are close, albeit the latter catalyst is slightly more active for OER. However, Figure 9b clearly indicates that the Ir catalysts at Pts@HCNS@Irs are electrocatalytically active for OER compared to the Pt/C catalysts. The results shown in Figure 9 successfully demonstrate the utility of Pts@HCNS@Irs as bifunctional electrocatalysts for ORR and OER. The separation of two different active catalysts, such as Pt and Ir, by carbon layers enables preserving their unique electrocatalytic activities, whereas the interaction between two catalysts results in the loss of activity as observed for ORR.

CONCLUSION

In summary, in the course of a study on galvanic replacement reactions involving manganese oxide, we realized that the use of carbon-encapsulated MnO nanoparticles as a template led to site-specific deposition of Pt nanocrystals on the outermost surfaces of the surrounding carbon shells. Exploiting the discovered process, we demonstrated a method for selectively decorating the external surfaces of the HCNSs with high densities of catalytic nanocrystals of various noble metals, including Pt, Pd, Rh, and Ir. Furthermore, this process was extended into a protocol of separately decorating the interior and exterior surfaces with a wide range of catalytic species, which may enable us to control and systematically integrate the catalytic functionalities of the specific surfaces of HCNSs.

METHODS

General Considerations. All reagents including $MnCl_2 \cdot 4H_2O$ (Kanto), sodium oleate (TCI), 1-octadecene (Aldrich), Igepal CO-520 (Aldrich), tetraethyl orthosilicate (Acros), NH_4OH (Samchun chem.), sodium hydroxide (Samchun chem.), HNO_3 (Samchun chem.), dopamine hydrochloride (Aldrich), Trizma base (Aldrich), hydrochloric acid (Samchun chem.), $Na_2PdCl_4 \cdot 3H_2O$ (Strem), $Na_2PtCl_4 \cdot xH_2O$ (Strem), $RhCl_3 \cdot xH_2O$ (Strem), $IrCl_3 \cdot xH_2O$ (Strem), and $RuCl_3 \cdot xH_2O$ (Strem) were used as purchased without any purification. Analyses of TEM images were conducted with a JEOL JEM-2100 and a JEM-ARM200F. SEM images were captured with a XL30S FEG field-emission scanning electron microscope (Philips electron optics, Netherlands). X-ray diffraction patterns were obtained using an X-ray diffractometer (18 kW) (Rigaku MAX-2500, Japan). Element analysis was performed using an Elementar vario EL III elemental analyzer. The contents of the metal elements in the nanoparticles were measured by inductive coupling plasma atomic emission spectrometry (ICPS-7500, Japan). Raman scattering measurements were performed using a micro-Raman spectroscopy system equipped with a CCD detector (Acton SP2300, Princeton Instruments, America).

Preparation of MnO@C. Surfactant-free Mn_3O_4 nanoparticles were prepared in advance by following a previously reported method.[17] Ten milligrams of Mn_3O_4 nanoparticles was immersed in 16.4 mL of tris(hydroxymethyl)aminomethane (Tris) buffer solution (10 mM, pH 8.5) containing 0.61 mg/mL of dopamine and stirred in the air at room temperature for 24 h. The resulting Mn_3O_4@PDA nanoparticles were isolated from the suspension by centrifugation and then washed several times by repeating the dispersion in distilled water and centrifugation. The purified solids of the Mn_3O_4@PDA nanoparticles were dried in a convection oven at 70 °C for 12 h. The completely dried solids were placed in a tube-type furnace, heated at a rate of 5 °C/min, and annealed at 500 °C for 5 h under a flow of Ar + 4% H_2, producing the solid MnO@C, which consisted of reduced MnO cores and carbon shells.

Deposition of Pt Nanocrystals on the Surfaces of MnO@C: Preparation of MnO@C@Pts. MnO@C nanoparticles (3.0 mg) were immersed in 3 mL of an aqueous solution of Na_2PtCl_4 (5.0 mg/mL), the pH of which was adjusted to 3.2 by the addition of diluted HCl solution, and stirred at 100 °C for 12 h. After being cooled to room temperature, the resulting MnO@C@Pts was isolated by centrifugation and purified by repeating the dispersion in an aqueous suspension and centrifugation three times. To investigate the progress of the reaction by acquiring TEM images and determining the Mn and Pt contents of the resulting nanoparticles, 0.5 mL of suspension was removed from the reaction suspensions at various reaction times (5 min, 10 min, 20 min, 30 min, 1 h, and 4 h), and the solid samples were recovered from each suspension by centrifugation.

For the control experiment without the Pt precursor, 1 mg of MnO@C was dissolved in a diluted HCl solution (pH 3.2) and stirred at 100 °C for 12 h. After being cooled to room temperature, the resulting nanoparticles were collected by centrifugation and washed three times with water.

Investigation of the Enhanced Acid Resistance of MnO@C. In order to verify the improved stability of the MnO cores encapsulated by the carbon shells, MnO@C nanoparticles (1 mg) were immersed

into 1 mL of HCl solution (pH 1.4) and stirred at room temperature for 24 h. The acid-treated nanoparticles were retrieved by centrifugation and purified by repeating the dispersion in an aqueous suspension and centrifugation three times. For control purposes, MnO@SiO_2 and MnO@Mn_3O_4 nanoparticles without carbon shells were prepared by following the previously reported procedure and then treated in HCl solutions using the same procedure as that applied for the MnO@C.[40,41] In the case of the experiment with MnO@Mn_3O_4, the nanoparticles were completely dissolved during the acid treatment and any solid was not precipitated by centrifugation.

Control Experiments with Hollow Carbon Nanospheres Instead of MnO@C. In order to prepare the hollow carbon nanospheres, which were used in the control experiment, 3 mg of MnO@C was dispersed in 3 mL of HNO_3 solution (0.1 M) and stirred for 12 h at room temperature. The resulting hollow carbon nanoparticles were collected by centrifugation and washed three times with water. The resulting hollow carbon spheres (1 mg) were added together with $MnCl_2$ (1 mg) to 1 mL of an aqueous solution of Na_2PtCl_4 (5.0 mg/mL), the pH of which was adjusted to 3.2 by the addition of diluted HCl solution, and reacted at 100 °C for 12 h with constant stirring. After being cooled to room temperature, the resulting particles were isolated by centrifugation and then purified by repeating the dispersion in an aqueous suspension and centrifugation three times. Another control experiment with hollow carbon nanospheres was carried out by using the supernatant solution obtained after treating MnO@C (1 mg) in an HCl solution (pH 3.2), instead of the $MnCl_2$ solution, at 100 °C for 12 h and then removing the remaining solids by centrifugation.

Control Experiments with Mn_3O_4@C Instead of MnO@C. The Mn_3O_4@C nanospheres used for the control experiment were prepared by oxidizing MnO@C nanoparticles under hydrothermal conditions. For this, MnO@C (10 mg) was dispersed into an aqueous suspension (10 mL) in a 50 mL stainless steel autoclave with a Teflon chamber and reacted at 200 °C for 20 h. After being cooled to room temperature, the resulting Mn_3O_4@C nanoparticles were collected by centrifugation and purified by twice repeating the dispersion in an aqueous suspension and centrifugation. The Pt growth reactions were carried out using a similar procedure as that applied for the synthesis of MnO@C@Pt; 0.3 mL of Mn_3O_4@C (1 mg/mL) was mixed with 1 mL of an aqueous solution of Na_2PtCl_4 (3.0 mg/mL), the pH of which was adjusted to 2.4 by the addition of diluted HCl solution (total reaction volume: 3 mL), and stirred at 70 °C for 2 h. After being cooled to room temperature, the resulting product was isolated by centrifugation and purified by repeating the dispersion in an aqueous suspension and centrifugation three times.

Experiments for Investigating the Effect of the Shell Thickness of the MnO@C. For the preparation of the Mn@C with 3.1 (±0.3) nm and 4.9 (±0.4) nm carbon-shell thicknesses, MnO@PDA was synthesized in solutions containing 0.15 and 0.30 mg/mL of dopamine, respectively. Except for the dopamine concentration in the preparation of the MnO@PDA, all reaction conditions were the same as those applied for the preparation of MnO@C with shell thicknesses of 7.6 (±0.9) nm. Galvanic replacement reactions were carried out in solutions containing 1.0 mg/mL of MnO@C and 5 mg/mL of Na_2PtCl_4 at 70 °C and pH 3.2.

Preparation of HCNS@Ms (M = Pt, Pd, Ir, and Rh). For the preparation of HCNS@Pts by dissolving the remaining MnO cores, 1 mg of MnO@C@Pts was immersed in 5 mL of HNO_3 solution (0.1 M) and stirred overnight at room temperature. The resulting HCNS@Pts nanoparticles were collected by centrifugation and washed with water by repeating the dispersion in an aqueous suspension and centrifugation three times. The existence of the void spaces inside the HCNS@Pts nanoparticles was verified by removing the deposited Pt nanocrystals of the HCNS@Pts by treatment with 12 M HCl solution for 12 h and analyzing TEM images of the resulting hollow carbon nanospheres.

The preparations of MnO@C@Pds, MnO@C@Irs, and MnO@C@Rhs were conducted by immersing 1 mg of MnO@C in Na_2PdCl_4 (1 mL, 5 mg/mL, pH 3.8), $IrCl_3$ (1 mL, 1 mg/mL, pH 2.6), and $RhCl_3$ (1 mL, 1 mg/mL, pH 2.6), respectively, and stirring for 12 h at 100 °C. The pH was adjusted by the addition of diluted HCl solution. After being cooled to room temperature, the resulting MnO@C@Ms (M = Pd, Ir, and Rh) nanoparticles were collected by centrifugation and purified by repeating the dispersion in an aqueous suspension and centrifugation three times. The HCNS@Ms (M = Pd, Ir, and Rh) were prepared by removing the MnO cores from the MnO@C@Ms (M = Pd, Ir, and Rh) using the same procedure as that applied for preparing HCNS@Pts.

Deposition of Metal Nanocrystals on the Interior Surfaces of HCNSs: Preparation of Pts@HCNS. The synthesis of Mn_3O_4@Pts, which immobilized large numbers of Pt nanocrsytals on the surfaces of Mn_3O_4 nanoparticles, was carried out through the reported procedure, which included the reaction of surfactant-free Mn_3O_4 (10 mg) in 10 mL of an aqueous solution of Na_2PtCl_4 (5 mg/mL) at 70 °C for 30 min.[17] The deposition of the PDA film on the Mn_3O_4@Pts was followed by carbonization, which generated the MnO@Pts@C, and was performed using the same procedure as that applied for the synthesis of MnO@C. The resulting MnO@Pts@C was immersed in a 0.1 M HNO_3 solution and stirred overnight at room temperature to remove the MnO cores, resulting in the formation of Pts@HCNS. The Pts@HCNS was separated by centrifugation and purified by repeating the dispersion in an aqueous suspension and centrifugation three times.

Deposition of Metal Nanocrystals on the Exterior Surfaces of MnO@Pts@C: Preparation of Pts@HCNS@Ms (M = Pt, Pd, Ir, and Rh). The deposition of metal nanocrystals on the external surfaces of MnO@Pts@C was carried out using a similar procedure as that applied for the synthesis of MnO@C@Ms (M = Pt, Pd, Ir, and Rh), except for the use of MnO@Pts@C instead of MnO@C. For the deposition of Pt and Ir nanocrystals, 1 mg of MnO@Pts@C was added into Na_2PtCl_4 (1 mL, 5 mg/mL) and $IrCl_3$ (1 mL, 5 mg/mL) solutions containing 0.07 mL of 12 mM HCl and then stirred at 100 °C for 4 h, which produced Pts@HCNS@Pts and Pts@HCNS@Irs, respectively. For the preparation of Pts@HCNS@Pds, 1 mg of MnO@Pts@C was immersed into an aqueous solution of Na_2PdCl_4 (1 mL, 3 mg/mL) at 40 °C and stirred for 2 h. Pts@HCNS@Rhs was prepared by adding 1 mg of MnO@Pts@C to 1 mL of an aqueous solution of $RhCl_3$ (0.5 mg/mL) and stirred at 70 °C for 10 h. The resulting Pts@HCNS@Ms (M = Pt, Pd, Ir, and Rh) nanoparticles were retrieved by centrifugation and purified by repeating the dispersion in an aqueous suspension and centrifugation three times.

Preparation of Pts@HCNS@Irs Nanoparticles for Electrocatalytic Experiments. In order to prepare the Pts@HCNS@Irs (Pt/Ir = 1:1 in atomic ratio) used for the electrocatalytic experiments, MnO@Pts@C, which was derived by annealing Mn_3O_4@Pts@PDA at 700 °C for 4 h under a flow of Ar + 4% H_2, was immersed in an aqueous solution of $IrCl_3$ (1 mg/mL), the pH of which was adjusted by adding 0.07 mL of 12 mM HCl, and stirred at 50 °C for 4 h. For the synthesis of HCNS@(Pt/Ir)s (Pt/Ir = 1:1 in atomic ratio), which was used as a control, the MnO@C was prepared by annealing Mn_3O_4@Pts@PDA at 700 °C for 4 h under a flow of Ar + 4% H_2 and then treating it in a solution containing Na_2PtCl_4 (1 mg/mL) and $IrCl_3$ (1 mg/mL) at 50 °C and pH 3.4 for 4 h.

Reagents and Instruments for the Electrochemical Study. All reagents, including Pt/C catalysts (20 wt % Pt on carbon support, Alfa Aesar, HiSPEC fuel-cell grade), Nafion solution (Sigma), and $HClO_4$ (Merck), were used as purchased without any purification, and 0.1 M $HClO_4$ was used as a supporting electrolyte solution. Electrochemical measurements were performed using a CHI 660D (CH Instrument) potentiostat. A Pt wire and Ag/AgCl electrodes (3 M KCl) were used as the counter and reference electrodes, respectively. A glassy carbon rotating disk electrode (GC RDE, d = 5 mm, Pine Instrumentation) was used as a working electrode. The rotating disk electrode data for ORR polarization curves were obtained using a Pine Model MSRX rotator.

Electrochemical Measurements. An aqueous dispersion of each catalyst was sonicated for 15 min, and a portion of the dispersion was then dropped onto the GC RDE (A = 0.196 cm^2). The amount of Pt and It catalysts loaded on a GC RDE are 15.3 and 15.0 $\mu g/cm^2$, respectively. After drying under air for 2 h, the electrode was covered with 15 μL of Nafion solution (0.05 wt %), followed by the evaporation of water and vacuum treatment for 30 min prior to the electrochemical measurement. The ORR polarization curves were obtained using O_2-saturated 0.1 M

$HClO_4$ electrolyte solutions using the catalyst-loaded GC RDEs, at a rotation rate of 1600 rpm and a scan rate of 10 mV/s. Before obtaining the ORR polarization curves, the electrode was subjected to several potential cycling steps between −0.06 and 1.26 V to clean the electrode surface. Linear sweep voltammograms for OER were obtained in a N_2-saturated 0.1 M $HClO_4$ at a rotation rate of 1600 rpm and a scan rate of 10 mV/s.

Conflict of Interest: The authors declare no competing financial interest.

Acknowledgment. This work was supported by the National Research Foundation of Korea (NRF) grant funded by the Korea government (MEST) (2011-0017377) (I.S.L.) and (2012R1A1A2041671) (J.K.).

Supporting Information Available: More experimental data including Raman spectrum, TEM images, and cyclic voltammograms (Figures S1−S6). This material is available free of charge *via* the Internet at http://pubs.acs.org.

REFERENCES AND NOTES

1. Zhu, J.; Holmen, A.; Chen, D. Carbon Nanomaterials in Catalysis: Proton Affinity, Chemical and Electronic Properties, and Their Catalytic Consequences. *ChemCatChem* **2013**, *5*, 378–401.
2. Antolini, E. Carbon Supports for Low-Temperature Fuel Cell Catalysts. *Appl. Catal., B* **2009**, *88*, 1–24.
3. Campelo, J. M.; Luna, D.; Luque, R.; Marinas, J. M.; Romero, A. A. Sustainable Preparation of Supported Metal Nanoparticles and Their Applications in Catalysis. *ChemSusChem* **2009**, *2*, 18–45.
4. Fang, X.; Zhao, X.; Fang, W.; Chen, C.; Zheng, N. Self-Templating Synthesis of Hollow Mesoporous Silica and Their Applications in Catalysis and Drug Delivery. *Nanoscale* **2013**, *5*, 2205–2218.
5. Li, X.; Yang, Y.; Yang, Q. Organo-Functionalized Silica Hollow Nanospheres: Synthesis and Catalytic Application. *J. Mater. Chem. A* **2013**, *1*, 1525–1535.
6. Liu, J.; Qiao, S. Z.; Chen, J. S.; Lou, X. W.; Xing, X.; Lu, G. Q. Yolk/Shell Nanoparticles: New Platforms for Nanoreactors, Drug Delivery and Lithium-Ion Batteries. *Chem. Commun.* **2011**, *47*, 12578–12591.
7. Böttger-Hiller, F.; Kempe, P.; Cox, G.; Panchenko, A.; Janssen, N.; Petzold, A.; Thurn-Albrecht, T.; Borchardt, L.; Rose, M.; Kaskel, S.; *et al.* Twin Polymerization at Spherical Hard Templates: An Approach to Size-Adjustable Carbon Hollow Spheres with Micro- or Mesoporous Shells. *Angew. Chem., Int. Ed.* **2013**, *52*, 6088–6091.
8. Fang, Y.; Guo, S.; Li, D.; Zhu, C.; Ren, W.; Dong, S.; Wang, E. Easy Synthesis and Imaging Applications of Cross-Linked Green Fluorescent Hollow Carbon Nanoparticles. *ACS Nano* **2012**, *6*, 400–409.
9. Zhang, C.; Wu, H. B.; Yuan, C.; Guo, Z.; Lou, X. W. Confining Sulfur in Double-Shelled Hollow Carbon Spheres for Lithium−Sulfur Batteries. *Angew. Chem., Int. Ed.* **2012**, *51*, 9592–9595.
10. Tan, Y.; Xu, C.; Chen, G.; Fang, X.; Zheng, N.; Xie, Q. Facile Synthesis of Manganese-Oxide-Containing Mesoporous Nitrogen-Doped Carbon for Efficient Oxygen Reduction. *Adv. Funct. Mater.* **2012**, *22*, 4584–4591.
11. Galeano, C.; Baldizzone, C.; Bongard, H.; Spliethoff, B.; Weidenthaler, C.; Meier, J. C.; Mayrhofer, K. J. J.; Schüth, F. Carbon-Based Yolk−Shell Materials for Fuel Cell Applications. *Adv. Funct. Mater.* **2013**, *24*, 220–232.
12. Schaefer, Z. L.; Gross, M. L.; Hickner, M. A.; Schaak, R. E. Uniform Hollow Carbon Shells: Nanostructured Graphitic Supports for Improved Oxygen-Reduction Catalysis. *Angew. Chem., Int. Ed.* **2010**, *49*, 7045–7048.
13. Harada, T.; Ikeda, S.; Hashimoto, F.; Sakata, T.; Ikeue, K.; Torimoto, T.; Matsumura, M. Catalytic Activity and Regeneration Property of a Pd Nanoparticle Encapsulated in a Hollow Porous Carbon Sphere for Aerobic Alcohol Oxidation. *Langmuir* **2010**, *26*, 17720–17725.
14. Ding, Y.; Jin, B.; Gu, G.; Xia, X.-H. One-Step Pyrolysis Method for the Synthesis of Highly Efficient 3D Hollow Carbon Nanostructure Supported Metallic Catalysts. *J. Mater. Chem.* **2009**, *19*, 9141–9146.
15. Harada, T.; Ikeda, S.; Ng, Y. H.; Sakata, T.; Mori, H.; Torimoto, T.; Matsumura, M. Rhodium Nanoparticle Encapsulated in a Porous Carbon Shell as an Active Heterogeneous Catalyst for Aromatic Hydrogenation. *Adv. Funct. Mater.* **2008**, *18*, 2190–2196.
16. Kim, S. M.; Jeon, M.; Kim, K. W.; Park, J.; Lee, I. S. Postsynthetic Functionalization of a Hollow Silica Nanoreactor with Manganese Oxide-Immobilized Metal Nanocrystals Inside the Cavity. *J. Am. Chem. Soc.* **2013**, *135*, 15714–15717.
17. Kim, K. W.; Kim, S. M.; Choi, S.; Kim, J.; Lee, I. S. Electroless Pt Deposition on Mn_3O_4 Nanoparticles *via* the Galvanic Replacement Process: Electrocatalytic Nanocomposite with Enhanced Performance for Oxygen Reduction Reaction. *ACS Nano* **2012**, *6*, 5122–5129.
18. Sun, Y. Metal Nanoplates on Semiconductor Substrates. *Adv. Funct. Mater.* **2010**, *20*, 3646–3657.
19. Sun, Y.; Mayers, B.; Xia, Y. Metal Nanostructures with Hollow Interiors. *Adv. Mater.* **2003**, *15*, 641–646.
20. Wang, D.; Hisatomi, T.; Takata, T.; Pan, C.; Katayama, M.; Kubota, J.; Domen, K. Core/Shell Photocatalyst with Spatially Separated Co-catalysts for Efficient Reduction and Oxidation of Water. *Angew. Chem., Int. Ed.* **2013**, *52*, 11252–11256.
21. Liu, R.; Mahurin, S. M.; Li, C.; Unocic, R. R.; Idrobo, J. C.; Gao, H.; Pennycook, S. J.; Dai, S. Dopamine as a Carbon Source: The Controlled Synthesis of Hollow Carbon Spheres and Yolk-Structured Carbon Nanocomposites. *Angew. Chem., Int. Ed.* **2011**, *50*, 6799–6802.
22. Postma, A.; Yan, Y.; Wang, Y.; Zelikin, A. N.; Tjipto, E.; Caruso, F. Self-Polymerization of Dopamine as a Versatile and Robust Technique To Prepare Polymer Capsules. *Chem. Mater.* **2009**, *21*, 3042–3044.
23. Kong, J.; Yee, W. A.; Yang, L.; Wei, Y.; Phua, S. L.; Ong, H. G.; Ang, J. M.; Li, X.; Lu, X. Highly Electrically Conductive Layered Carbon Derived from Polydopamine and Its Functions in SnO_2-Based Lithium Ion Battery Anodes. *Chem. Commun.* **2012**, *48*, 10316–10318.
24. Ferrari, A. C.; Robertson, J. Interpretation of Raman Spectra of Disordered and Amorphous Carbon. *Phys. Rev. B* **2000**, *61*, 14095–14107.
25. Kaufman, J. H.; Metin, S. Symmetry Breaking in Nitrogen-Doped Amorphous Carbon: Infrared Observation of the Raman-Active G and D Bands. *Phys. Rev. B* **1989**, *39*, 13053–13060.
26. Li, S.-R.; Sun, Y.; Ge, S.-Y.; Qiao, Y.; Chen, Y.-M.; Lieberwirth, I.; Yu, Y.; Chen, C.-H. A Facile Route To Synthesize Nano-MnO/C Composites and Their Application in Lithium Ion Batteries. *Chem. Eng. J.* **2012**, *192*, 226–231.
27. Qiu, D.; Ma, L.; Zheng, M.; Lin, Z.; Zhao, B.; Wen, Z.; Hu, Z.; Pu, L.; Shi, Y. MnO Nanoparticles Anchored on Graphene Nanosheets *via In Situ* Carbothermal Reduction as High-Performance Anode Materials for Lithium-Ion Batteries. *Mater. Lett.* **2012**, *84*, 9–12.
28. Yao, T.; Cui, T.; Wu, J.; Chen, Q.; Yin, X.; Cui, F.; Sun, K. Preparation of Acid-Resistant Core/Shell Fe_3O_4@C Materials and Their Use as Catalyst Supports. *Carbon* **2012**, *50*, 2287–2295.
29. Herrmann, I. K.; Grass, R. N.; Mazunin, D.; Stark, W. J. Synthesis and Covalent Surface Functionalization of Non-oxidic Iron Core−Shell Nanomagnets. *Chem. Mater.* **2009**, *21*, 3275–3281.
30. Bratsch, S. G. Standard Electrode Potentials and Temperature Coefficients in Water at 298.15 K. *J. Phys. Chem. Ref. Data* **1989**, *18*, 1–21.
31. Bokhonov, B. B. Deposition of Platinum on the Outer Surface of Carbon-Encapsulated Silver Nanoparticles. *Carbon* **2011**, *49*, 2444–2449.
32. Guo, S.; Zhang, S.; Sun, S. Tuning Nanoparticle Catalysis for the Oxygen Reduction Reaction. *Angew. Chem., Int. Ed.* **2013**, *52*, 8526–8544.
33. Wu, J.; Yang, J. Platinum-Based Oxygen Reduction Electrocatalysts. *Acc. Chem. Res.* **2013**, *8*, 1848–1857.

34. Debe, M. K. Electrocatalyst Approaches and Challenges for Automotive Fuel Cells. *Nature* **2012**, *486*, 43–51.
35. Guo, S.; Wang, E. Noble Metal Nanomaterials: Controllable Synthesis and Application in Fuel Cells and Analytical Sensors. *Nano Today* **2011**, *6*, 240–264.
36. Park, S.; Shao, Y.; Liu, J.; Wang, Y. Oxygen Electrocatalysts for Water Electrolyzers and Reversible Fuel Cells: Status and Perspective. *Energy Environ. Sci.* **2012**, *5*, 9331–9344.
37. Cruz, J. C.; Baglio, V.; Siracusano, S.; Ornelas, R.; Arriaga, L. G.; Antonucci, V.; Aricò, A. S. Nanosized Pt/IrO_2 Electrocatalyst Prepared by Modified Polyol Method for Application as Dual Function Oxygen Electrode in Unitized Regenerative Fuel Cells. *Int. J. Hydrogen Energy* **2012**, *37*, 5508–5517.
38. Kitchin, J. R.; Nørskov, J. K.; Barteau, M. A.; Chen, J. G. Modification of the Surface Electronic and Chemical Properties of Pt(111) by Subsurface 3D Transition Metals. *J. Chem. Phys.* **2004**, *120*, 10240–10246.
39. Gasteiger, H. A.; Kocha, S. S.; Sompalli, B.; Wagner, F. T. Activity Benchmarks and Requirements for Pt, Pt-Alloy, and Non-Pt Oxygen Reduction Catalysts for PEMFCs. *Appl. Catal., B* **2005**, *56*, 9–35.
40. Anisur, R. M.; Shin, J.; Choi, H. H.; Yeo, K. M.; Kang, E. J.; Lee, I. S. Hollow Silica Nanosphere Having Functionalized Interior Surface with Thin Manganese Oxide Layer: Nanoreactor Framework for Size-Selective Lewis Acid Catalysis. *J. Mater. Chem.* **2010**, *20*, 10615–10621.
41. Shin, J. M.; Anisur, R. M.; Ko, M. K.; Im, G. H.; Lee, J. H.; Lee, I. S. Hollow Manganese Oxide Nanoparticles as Multifunctional Agents for Magnetic Resonance Imaging and Drug Delivery. *Angew. Chem., Int. Ed.* **2009**, *48*, 321–324.